Optimal interferometric data acquisition and processing: towards 0.1% precision with the single-mode beam combiner VINCI

Pierre Kervella[a,b], Vincent Coudé du Foresto[a], Damien Ségransan[c] and Emmanuel Di Folco[d]

[a] LESIA, UMR 8109, Observatoire de Paris-Meudon, F-92195 Meudon Cedex, France;
[b] European Southern Observatory, Alonso de Cordova 3107, Vitacura, Santiago, Chile;
[c] Observatoire de Genève, CH-1290 Sauverny, Switzerland;
[d] European Southern Observatory, Karl-Schwarzschildstr. 2, D-85748 Garching, Germany.

ABSTRACT

Though interferometric techniques are now used routinely around the world, the processing of interferometric data is still the subject of active research. In particular, the corruption of the interferometric fringes by the turbulent atmosphere is currently the most critical limitation to the precision of the ground-based interferometric measurements. In this paper, we discuss the data acquisition and processing procedures of the VINCI/VLTI instrument. Optimal data acquisition parameters and wavelets based processing allow us to remove a posteriori part of the data corrupted by atmospheric turbulence. A relative precision better than 0.1% on the instrumental visibility (for a 5 minutes observation) was already achieved on bright stars without fringe stabilization. Using a dedicated fringe tracker, an even better precision, of the order of a few 10^{-4}, appears to be within reach. However, we show in this paper that the calibration of the instrumental visibility measurements can easily be the source of significant systematic errors beyond this statistical precision.

Keywords: interferometry, single-mode fibers, wavelets, signal processing

1. INTRODUCTION

Installed at the heart of the Very Large Telescope Interferometer (VLTI), the VINCI instrument combines coherently the infrared light coming from two telescopes in the infrared H and K bands. The first fringes were obtained in March 2001 with the VLTI Test Siderostats, and in October of the same year with the 8m Unit Telescopes (UTs). In order to reduce the large quantity of data produced by this instrument, we have developed innovative interferometric data analysis methods, using in particular the wavelet transform. We have appplied them successfully to a broad range of interferometric observations obtained with very different configurations of the VLTI (0.35 m siderostats, 8 m Unit Telescopes, 16 m to 140 m baselines, K and H band observations). Since the first fringes of VINCI, more than 800 nights of observations have been conducted with this instrument. This allowed to record a large number of individual star observations, under extremely different atmospheric and instrumental conditions. The data processing methods that are described in the present paper were successfully applied to all these configurations, and consistently provided reliable and precise results. This gives us good confidence that they are efficient and robust, and can be generalized to other interferometric instruments.

2. INSTRUMENTAL COHERENCE FACTOR

2.1. Instrument principle and raw signals

A detailed description of the VINCI instrument, including its hardware and software design, can be found in ([13]). Once the stellar light from the two telescopes has been injected into single mode optical fibers, it is recombined in a fiber based triple coupler called MONA. VINCI is based on the same principle as the FLUOR[7] instrument, and recombines the light through single mode fluoride glass optical fibers that are optimized for K band operation ($\lambda = 2.0 - 2.4$ μm). It uses in general a regular K band filter, but can also observe in the H

Send correspondence to P.K.: E-mail: pierre.kervella@obspm.fr

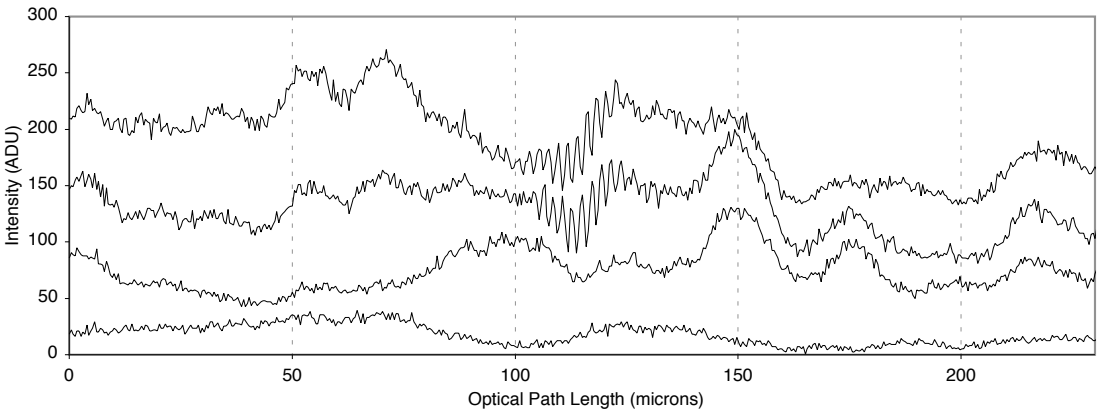

Figure 1. The raw signals I_1, I_2, P_A and P_B, for one interferogram obtained on θ Cen. The original signals have been translated vertically respectively by +90, +40, +40 and 0 ADUs for clarity.

band ($\lambda = 1.4 - 1.8$ μm) using an integrated optics beam combiner ([3]). The first observations with this new generation coupler installed at the VLTI focus have given promising results ([14];[12]).

Fig. 1 shows the raw signals of one interferogram obtained on the K giant θ Cen, of average quality in terms of injected flux stability. The photometric fluctuations are clearly visible on all four channels, while the interference fringes are located close to the center of the scan. The fringes are naturally in phase opposition between the two channels I_1 and I_2.

2.2. Fringe processing

The photometric calibration of the interferograms produced by VINCI is achieved using the two photometric control signals P_A and P_B and the κ-matrix. The calibration is computed separately for the I_1 and I_2 channels using the following formulae (see[4] for its derivation):

$$I_{1\,cal} = \frac{1}{2\,\sqrt{\kappa_{1,A}\;\kappa_{1,B}}} \frac{I_1 - \kappa_{1,A}P_A - \kappa_{1,B}P_B}{[\sqrt{P_A\;P_B}]_{\rm Wiener}} \tag{1}$$

$$I_{2\,cal} = \frac{1}{2\,\sqrt{\kappa_{2,A}\;\kappa_{2,B}}} \frac{I_2 - \kappa_{2,A}P_A - \kappa_{2,B}P_B}{[\sqrt{P_A\;P_B}]_{\rm Wiener}} \tag{2}$$

The subscript "Wiener" designates optimally filtered signals. This process allows first to subtract the photometric fluctuations that were introduced on the interferometric channels by the turbulent atmosphere (calibration), and then to normalize the resulting signals to the geometrical mean of the two photometric channels $P = \sqrt{P_A\;P_B}$. The Wiener filtering of P is essential to avoid numerical instabilities. After the normalization, $I_{1\ \rm cal}$ and $I_{2\ \rm cal}$ are apodized at their extremities, to prevent any edge effect during the numerical wavelet transform. Finally, these two signals are subtracted to obtain the interferometric signal I that is subsequently used to estimate the squared coherence factor of the fringes μ^2.

2.3. Estimation of the squared coherence factor μ^2

The goal of the interferometric data processing is to extract the squared visibility V^2 of the fringes. The intermediate step to this end is to measure the instrumental squared coherence factor μ^2 of the stellar light. This instrument dependent quantity characterizes the fraction of coherent light present in the total flux of the target. It is subsequently calibrated using observations of a known star, as described in Sect. 6, to derive the absolute visibility of the scientific target.

The average power spectral density of a sample observation of the dwarf star α Cen A, computed using the wavelet transform, is shown in Fig. 2. To obtain this 1D spectrum from the original 2D Wavelet Power Spectral

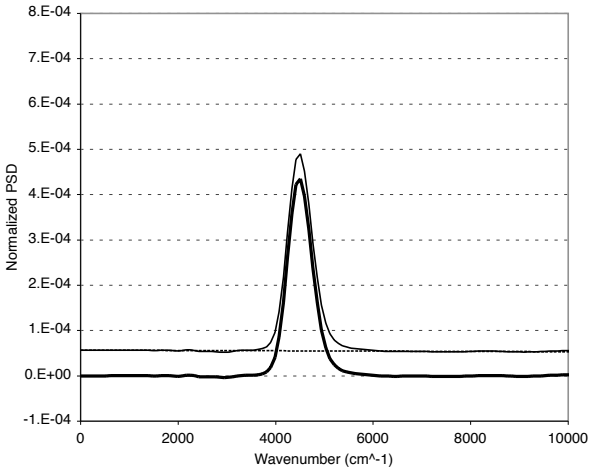

Figure 2. Average WPSD of a low visibility observation of α Cen A. The original two-dimensional matrix has been integrated over the fringe packet length in the time domain. The resulting projection on the wave number axis allows to visualize clearly the noise contribution. The subtracted noise model is shown by the dashed line. The final WPSD (thick line) shows no bias in spite of the large brightness of the star and very low squared coherence factor of the fringes ($\mu^2 \approx 0.3\,\%$).

Density (WPSD) matrices, we first project the WPSD matrix of each interferogram on the frequency axis, by integrating it over the fringe packet length (time axis). From this we obtain a series of one-dimensional vector PSDs, similar to the Fourier PSD but with a reduced noise. Before the averaging, we recenter each fringe peak using the frequency position information derived from the quality control of the interferograms (Sect. 4). This step allows to confine more tightly the energy of the peak, which is displaced by the first order piston effect. This reduces the influence of piston on the final μ^2 value. The co-added 1D spectrum is the signal used for the final power integration to estimate the μ^2 of the star.

2.4. Estimation of the statistical dispersion

To compute the statistical error on the μ^2 estimation, we integrate separately the fringe power for each interferogram of the batch, correct it from the detector and photon shot noise biases individually, and use a weighted bootstrapping technique on this set of measurements. Our sample is made of N pairs (μ_i^2, w_i) where μ_i^2 is the squared coherence factor obtained by integrating the WPSD of the scan of rank i in the series and w_i is its associated weight. It is defined as the average level of the photometric signal P over the fringe packet length (20 fringes in the K band) multiplied by the unbalance between the two photometric channels P_A and P_B:

$$w_i = \frac{\min(\overline{P_{A,i}}, \overline{P_{B,i}})}{\max(\overline{P_{A,i}}, \overline{P_{B,i}})} \; \overline{\left(\sqrt{P_{A,i} P_{B,i}}\right)}_{\text{Fringes}} \tag{3}$$

It characterizes well the clarity of the total photometric signal that contributes to the formation of the fringes. The final dispersion of the μ^2 values is reduced by this weighting.

The bootstrapping technique has the important advantage not to make any assumption on the type of statistical distribution that the data points follow. In particular, it is more reliable than the classical approach that assumes a gaussian distribution of the measurements. Skewness and other deviations from a gaussian distribution are automatically included in the error bars, which can be asymmetric.

3. STATISTICAL PRECISION LIMITING FACTORS

3.1. Detector and photon shot noise

The readout noise of the detector adds a constant variance to the recorded signals, that is of a larger relative amplitude for faint stars. In addition, the Poissonian nature of the photon signal adds a variable noise whose

variance is equal to the total number of collected photons. For faint stars, the photon shot noise is negligible compared to the detector noise, the opposite being true for bright stars. As demonstrated in ([19]) the photon shot noise is dominant compared to the detector noise almost up to the limiting magnitude of the instrument.

It does not appear possible to improve the *a posteriori* treatment of these two sources of noise, as they are intrinsic to the detection and to the signal itself, respectively. For this reason, we do not discuss them in the remainder of this paper. A discussion of the different types of noise intervening in the visibility measurements can be found for instance in ([6]) and ([18]).

3.2. Atmospheric piston

The photometric calibration of the interferograms compensates for the incidence of wavefront corrugation across each subpupil of the interferometer, however it does not help remove the random phase walk (differential piston) *between* the two subapertures. The differential piston, considered as a time-dependent OPD error $x(t)$, can be locally expressed by a polynomial development around a reference time t_0 (corresponding, for example, to the middle of the acquisition sequence):

$$x(t) = x_0 + \dot{x}\ (t - t_0) + \ddot{x}\ (t - t_0)^2 + ... \tag{4}$$

The effect of the OPD perturbation on the interferogram, and its consequence on the coherence factor measurement, depends on the order:

- **Zeroth order**: the constant term x_0 can be seen as a global offset of the fringe packet. It is detected and corrected by the QL algorithm which centers the fringe packet in the middle of the interferogram.
- **First order**: The first order of the piston $\dot{x}$ changes the fringe velocity and induces a simple frequency shift in the PSD. It modifies the fringe peak position, but acts only as a homothetic compression or expansion of the fringe packet along the OPD direction. The first order piston has no immediate effect on the fringe visibility. However, if the shifting speed $\dot{x}$ of the fringe packet is too high, it can result in an undersampling of the fringes that will affect the visibility.
- **Second and higher orders**: Any term of order two (*acceleration*) and beyond breaks the linear relationship in the scan between time and OPD, and consequently the Fourier relationship which is at the basis of the visibility calculation, distorting the shape of the fringe peak. This introduces a non-linear, seeing induced multiplicative noise on the visibility measurements, which is the dominant noise source for strong signals (bright objects).

Detailed studies of the properties of atmospheric piston can be found for example in ([17]) and ([9]).

4. QUALITY CONTROL OF THE INTERFEROGRAMS

4.1. Selected quality criteria

During the observations, a simple fringe packet centroiding algorithm is applied in near real-time to the raw data. The fringe packet center is localized with a precision of about one fringe (2 μm) after each scan and the resulting error is fed back to the VLTI delay lines as an OPD offset. This capability, called *fringe coherencing*, ensures that the residual OPD is less than a coherence length despite possible instrumental drifts. Yet, the correction rate (once per scan, i.e. a few Hz) is too slow to remove the differential piston mode of the turbulence. When a dedicated fringe tracking instrument becomes available on the VLTI (e.g. FINITO[10]), most of the piston will be actively removed by a servo loop. It remains to be checked how the residuals will still limit the final visibility precision. To avoid any bias on μ^2, we have to reject the interferograms that do not contain fringes (false detections), or whose fringes are severely corrupted by the atmospheric turbulence (photometrically or by the piston effect). The selection procedure is in practice similar to a shape recognition process.

For this purpose, we measure in the wavelet power spectral density (WPSD) the properties of the fringe peak both in the time and frequency domains, and we compare them with the expected properties of a reference interferogram of visibility unity, derived from the spectral transmission of the instrument. The fringe peak is

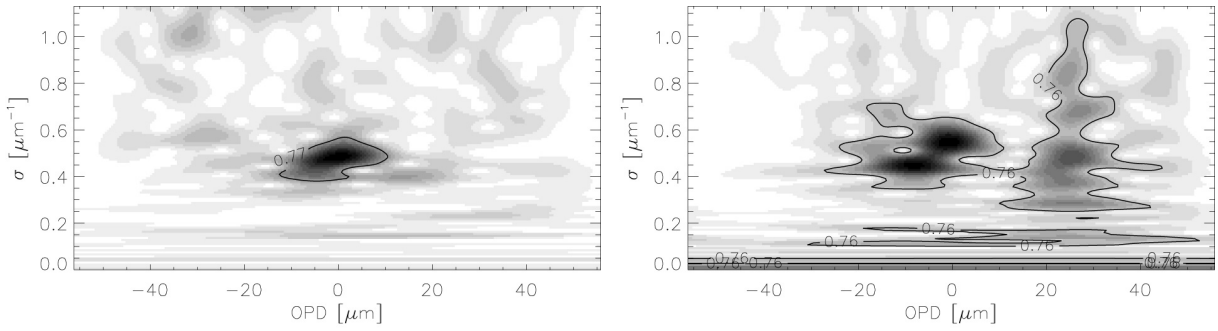

Figure 3. Wavelet power spectral densities of processed interferograms (σ represents the wave number, i.e. the inverse of the wavelength). The figure on the left shows the WPSD of a good quality interferogram: the energy is well confied in the fringe power peak. The WPSD on the right part of the figure is affected by strong atmospheric piston: a significant part of the fringe power is spread outside of the theoretical fringe peak, both in time and frequency domains. The isocontours delimit 77 % and 76 % of the total modulated power, respectively.

first localized in frequency by the maximum of the WPSD, and then the full width at half maximum is computed along the two directions: time and frequency. As the fringe packet has been recentered before the calibration, its position in the time domain is zero. Three parameters are then checked for quality:

- peak width in the time domain (typically ±50% around the theoretical value is acceptable),
- peak position in the frequency domain (±30%),
- peak width in the frequency domain (±40%).

In principle, the variation of the fringe contrast over the spectral band should also be taken into account in order to create the theoretical reference interferogram. But in practice, as long as the visibility of the fringes does not cancel out for a wavelength located inside the spectral band of the observations, the shape of the interferogram remains very close to theoretical fringes of visibility unity.

Fig 3 shows two examples of interferogram WPSD, one of them being affected by atmospheric piston. The difference in terms of fringe peak shape is clearly noticeable, and leads to the rejection of the corrupted interferogram (right part of the figure). This selection process has shown a very low false detection rate, and rejects efficiently the interferograms that are affected by a strong piston effect. However, limited piston of order two (and above) is not identified efficiently. The problem here is that the relevant properties for the estimation of the second order piston are currently difficult to measure with a sufficient SNR from the data, as they are masked by the order 1 piston. We expect that the introduction of the FINITO fringe tracker in 2004 will allow us to derive an efficient metric to reject the interferograms affected by high order piston effect.

4.2. Immunity to selection biases

An essential aspect of the parameters used for the quality control of the fringe peak properties is that they are largely independent from the visibility of the fringes, and therefore do not create selection biases. In particular, the integral of the fringe peak (directly linked to the visibility) or its height are never considered in the selection. The parameters chosen in Sect. 4 clearly depend on the photometric SNR, but are independent from the visibility of the fringes, thanks to the calibration procedure described in Sect. 2.

Fig. 4 demonstrates this independence in the difficult case of a very low contrast ($V^2 \leq 1\%$) batch of interferograms obtained on α Cen A. Despite the faintness of the fringes (and consequently the low correlated flux), no systematic deviation is visible for low photometric SNR values, as the dispersion is symmetric around the mean value. This means that the quality control described in this paragraph is not linked to the observable, and thus does not introduce a selection bias. A critical case is when the visibility is extremely low. In this situation, the fringe peak will tend to blend in with the noise, which tends to make it appear broader and

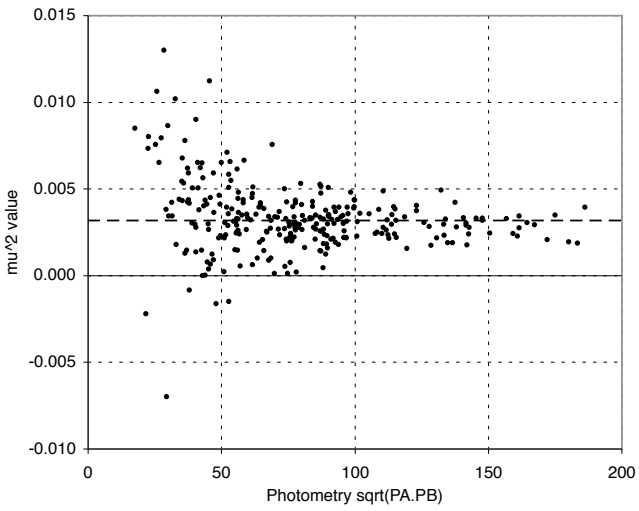

Figure 4. Squared coherence factor μ^2 as a function of the photometric signal on the fringe packet, for the very low contrast batch of interferograms obtained on $\alpha\,\mathrm{Cen\,A}$ ($V^2 \leq 1\%$). The dashed line show the mean value of the series derived using the bootstrap technique.

slightly displaced. Therefore, low-visibility data are more likely to be rejected than high-visibility data. This can introduce a bias towards higher μ^2 for low-visibility observations: a scan with a $+1\,\sigma$ deviation is accepted, but a scan with a $-1\,\sigma$ deviation is more likely to be rejected as it fails the selection criteria.

However, in this situation, the risk is high to fail to reject the spurious spikes that are created in the calibrated interferograms due to the division by the P signal (Sect. 2). Without the selection procedure, the modulated power of these calibration artefacts will be integrated in the final μ^2 value. As this power is essentially random, but always positive, these misidentifications would then result in a strong positive bias on the final μ^2 value. For this reason, and in spite of the potential rejection of a small part of the valid interferograms, the application of the selection procedure results in a more reliable estimate of μ^2, even for the very low visibility fringes. In any case, the careful examination of the statistical properties of the μ^2 histogram, and in particular of its skewness, allows to detect a possible selection bias.

5. STATISTICAL PRECISION ON μ^2 ACHIEVED WITH VINCI

The relative $1\,\sigma$ statistical error bar of a series of 100 reduced interferograms obtained with the 0.35 m aperture Test Siderostats is well approximated by the empirical expression:

$$\left[\frac{e\left(\mu^2\right)}{\mu^2}\right]_{\mathrm{Sid}} = 3.1\,10^{-3}\ \exp\left(0.78\ m_{K\mathrm{Corr}}\right) \tag{5}$$

Fig 5 shows the data used to derive this expression. They were obtained at a fringe frequency of 297 Hz, corresponding to a camera readout frequency of 1.5 kHz (5 samples/fringe). This relatively high frequency is commonly used at Paranal to minimize the effect of atmospheric piston on the fringe visibility. The correlated magnitude is defined as the photometric K magnitude of the star m_K, weighted by the squared coherence factor μ^2:

$$m_{K\mathrm{Corr}} = -2.5\log_{10}\left(\mu^2\ 10^{-m_K/2.5}\right) \tag{6}$$

The statistical dispersion shows two regimes: for bright stars ($m_{K\mathrm{Corr}} \leq 2$), the precision is flat and limited by the piston and photon shot noise, while for $m_{K\mathrm{Corr}} \geq 2$, the main contributor to the dispersion is the detector noise of the LISA camera, and the precision degrades rapidly. The general shape of this curve compare well with the results obtained by Tatulli et al. ([19]) . The smallest statistical dispersion obtained with VINCI for a single

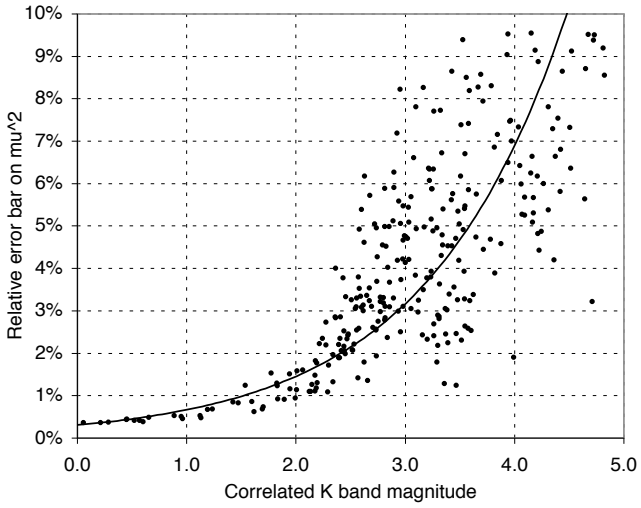

Figure 5. Relative error bars $e(\mu^2)/\mu^2$ of 296 individual VINCI stellar observations, normalized to a standard batch length of 100 interferograms. They were obtained with VINCI and the 0.35 m Test Siderostats of the VLTI, at a fringe frequency of 297 Hz, and represent a total of 98 936 processed interferograms. The horizontal axis is the correlated K band magnitude (see text). The curve represents the best fit exponential model, $e(\mu^2)/\mu^2 = 3.1\,10^{-3}\ \exp(0.78\ m_{K\mathrm{Corr}})$.

observation was recorded repeatedly on several nights during observations of the nearby dwarf Sirius (reported in[15]), with a relative error of only $\sigma(\mu)/\mu = \mathbf{0.08}\%$ for 5 minutes of continuous observations (500 interferograms).

The Auxiliary Telescopes, with their 1.8 m aperture, are expected to bring a gain of 2 to 3 magnitudes compared to the Siderostats, therefore shifting the precision curve by this ammount to the right of Fig. 5. The Unit Telescopes equipped with MACAO[2] adaptive optics will bring a sensitivity improvement of 6 to 7 magnitudes, assuming a Strehl ratio of 50 %. The fringe tracker FINITO[10] will cancel most of the piston noise, and therefore authorize the use of very slow scanning speeds. As a consequence, the μ^2 relative precision currently obtained only on the brightest sources ($\sigma(\mu)/\mu \simeq 0.1\,\%$ for 500 scans) will be achievable on all stars on whom FINITO will be able to track the fringes. However, the limiting magnitude will not be significantly improved as compared to VINCI alone. For bright stars, it is also expected that the relative dispersion of the μ^2 values will be diminished to a few 10^{-4}.

6. SYSTEMATIC CALIBRATION UNCERTAINTIES

The high precision measurement of the instrumental squared coherence factor μ^2 (down to a precision of $\sigma(\mu)/\mu \simeq 0.1\,\%$) is only the first step to obtain the absolute visibility V of the observed object. In this Section, we discuss the different sources of systematic uncertainty that are created by the instrument calibration process.

6.1. Principle of the visibility calibration

The data reduction software of VINCI yields accurate estimates of the squared modulus of the coherence factor μ^2, which is linked to the squared object visibility V^2 by the relation:

$$V^2 = \frac{\mu^2}{T^2} \tag{7}$$

where T^2 is the response of the system to a point source, also called transfer function (hereafter TF), interferometric efficiency, or system visibility. It is measured by bracketing the science target with observations of calibrator stars whose V^2 is supposed to be known a priori. The accuracy of our knowledge of the calibrator angular diameter, and the precision with which we estimate its μ^2 are therefore decisive for the final quality of the scientific target observation. Typically, the scientific targets are bracketed by calibrator observations, so as to be able to verify the stability of the TF.

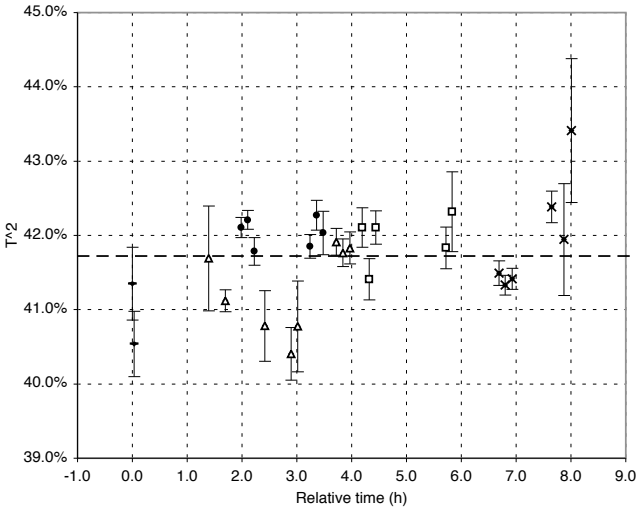

Figure 6. Evolution of the transfer function T^2 during one night (2002-05-29) on the E0-G0 baseline of the VLTI (16 m in ground length). Each symbol corresponds to a different star.

6.2. Interferometric transfer function estimation

By nature, the interferometric TF is affected by a large number of parameters: atmospheric conditions (seeing, coherence time), polarization (incidence of the stellar beams on the siderostat mirrors, spectrum of the target, etc...). These effects combine to make T^2 a stochastic variable, that can evolve over a wide range of timescales. In order to estimate its value and uncertainty on a particular date at which it was not directly measured (e.g. during the observation of a scientific target), it is necessary to use a model of its evolution. Such a model relies necessarily on an hypothesis, for instance that the value of T^2 is constant between two (or more) calibrator observations, that it varies linearily, quadratically, or any higher order model. Let us now evaluate the most suitable type of TF model for the observations with VINCI.

As a practical example, Fig. 6 shows the evolution of T^2 over one night of observations, with a typical sampling rate of one measurement every 15 minutes. This series of 27 observations was obtained during the night of 29 May 2003 on the E0-G0 baseline (16 m ground length). A number of different stars with known angular diameters were observed, covering spectral types in the G-K range. During these observations, spread over 8 hours, the seeing evolved from 1.0 to 2.0 arcsec, the altitude of the observed objects was distributed almost uniformly between 25 and 80 degrees, and the azimuth values covered 15 to 90 degrees (N = 0, E = 90). Due to this broad range of conditions, this series represents a worst case in terms of TF stability. Over the whole night, the overall stability is satisfactory, with a dispersion of $\sigma_{\rm tot} = 0.64\%$ around the average value of $\overline{T^2} = 41.75\%$. It is interesting to note that this dispersion is significantly larger than the smallest statistical dispersions observed with VINCI (down to $\sigma(\mu^2)/\mu^2 = 0.2\%$ over 5 minutes), and thus is a strong limitation of the final accuracy of the visibility estimate. The average precision of each individual T^2 measurement in our sample night is $\sigma_{\rm int} = 0.21\%$. This gives an external dispersion of $\sigma_{\rm ext} = 0.60\%$. In this particular case, the external dispersion is thus dominant over the internal measurement errors, by a factor of almost three.

From this example, we can conclude that the rate of one measurement every 15 minutes is insufficient to sample the fluctuations of the TF. Due to this, we do not gain in precision by interpolating the TF values using a high order model (quadratic, splines,...). In the current state of the VLTI (siderostat observations), the most adequate model for the estimation of the TF is thus a constant value between the observations of the calibrators. The 1.8 m Auxiliary Telescopes will soon allow to sample the TF with a much higher rate, of the order of 1 minute, and higher order models of the TF variations could become necessary. As we are dominated by the external dispersion $\sigma_{\rm ext}$, the uncertainty on the TF has to be estimated from the dispersion of the individual T^2 measurements obtained before and after the scientific target, without averaging of their associated error bars.

Under good and stable conditions, the random dispersion of T^2 introduced by the atmosphere can be very low between two consecutive observations of a calibrator. In this case, we want to evaluate the true uncertainty on the model T^2 by confronting the hypothesis of stability to the calibrator observations, and refine subsequently the hypothesis used to estimate the error bar on T^2. The observational strategy chosen with VINCI is to record several series of interferograms consecutively for each calibrator observation (typically three), over a period of about 15 minutes. To decide if the atmospheric and instrumental conditions are stable over this period, we compute the following χ^2 expression:

$$\chi^2_{\rm tot} = \sum_i \frac{(T^2_i - \overline{T^2})^2}{\sigma^2_{{\rm stat},i}} \tag{8}$$

where T^2_i are the consecutive estimates of the TF obtained on the calibrator, $\sigma^2_{{\rm stat},i}$ the statistical error of each measurement, and T^2 the weighted average of the T^2_i values (using the inverse of the statistical variance as weights). If the resulting χ^2 is small (less than 3), then the hypothesis that the TF is constant is probably true: the T^2_i values can be averaged and the global statistical error bar reduced accordingly. If not, then this hypothesis cannot be made, and a realistic approach is to consider as the true measurement error of the average TF the standard deviation of the T^2_i sample.

When several series of interferograms are obtained on the same calibrator and the conditions described above are verified, the resulting estimates of the TF can be averaged in order to reduce the attached statistical error bar. However, the systematic error introduced by the *a priori* uncertainty on the angular size of one calibrator cannot be reduced by repeatedly observing this star, but only by combining the TF measurements obtained on independent objects.

6.3. Calibrators angular size and intensity profile

Our *a priori* knowledge of the physical properties of a calibrator star is never perfect, and an uncertainty exists on its angular size and intensity profile. The real stellar intensity profiles are in general significantly different from the uniform disk model. Unfortunately, the visibility curve shape before the first minimum is almost impossible to distinguish between a UD and limb darkened disk (LD) model. Therefore, when we are measuring visibilities in the first lobe of the visibility function, it is necessary to use a model of the stellar disk limb darkening to recover the true photospheric angular size of the star. A classical approach is to make use of conversion factors $\theta_{\rm UD}/\theta_{\rm LD}$ ([8] ,[20]). This is a satisfactory approximation as long as the observed star is not resolved close to or beyond the first minimum of its visibility function. The intensity profiles are currently produced using radiative transfer computer codes, such as ATLAS ([16]) and PHOENIX ([11]). A rather complete database of intensity profiles can be found in ([5]). The limb darkening is in any case pretty small at infrared wavelengths (of the order of 2-3%), and the uncertainty introduced by the LD models on the angular diameter is expected to be significantly smaller than 0.5%. However, for visible-light measurements, the LD conversion factor can reach 10%, and significant biases at the level of several percents could be created.

6.4. Broadband visibility model

An important effect of the relatively large spectral bandwidth of the VINCI filter is that several spatial frequencies are observed simultaneously by the interferometer. This effect is called *bandwidth smearing*. While the question of the effective wavelength of broadband interferometric measurements has been studied since the early days of interferometry ([1]), the bandwidth smearing is different in essence. This effect is not related only to the incoming photons wavelength, but also to the variation of visibility over the observation bandwidth. Thus, it is naturally non linear, and cannot be characterized by a single number.

The left part of Fig. 7 shows the average WPSD of a series of interferograms of α Cen A obtained at very low contrast ($V^2 \leq 1\%$). The bandwidth smearing effect is particularly strong as the visibilities are close to the first minimum of the visibility function, and this effect cannot be neglected for this particular observation. With a 60 m projected baseline, the short wavelength edge of the K band ($\lambda \simeq 2.0\mu$m) is already at the null of visibility, while V^2 for the long wavelength edge ($\lambda \simeq 2.4\mu$m) is still above 1%. Therefore, the fringe peak becomes very asymmetric in the PSD of the interferograms. The observed and model PSDs agree well in general

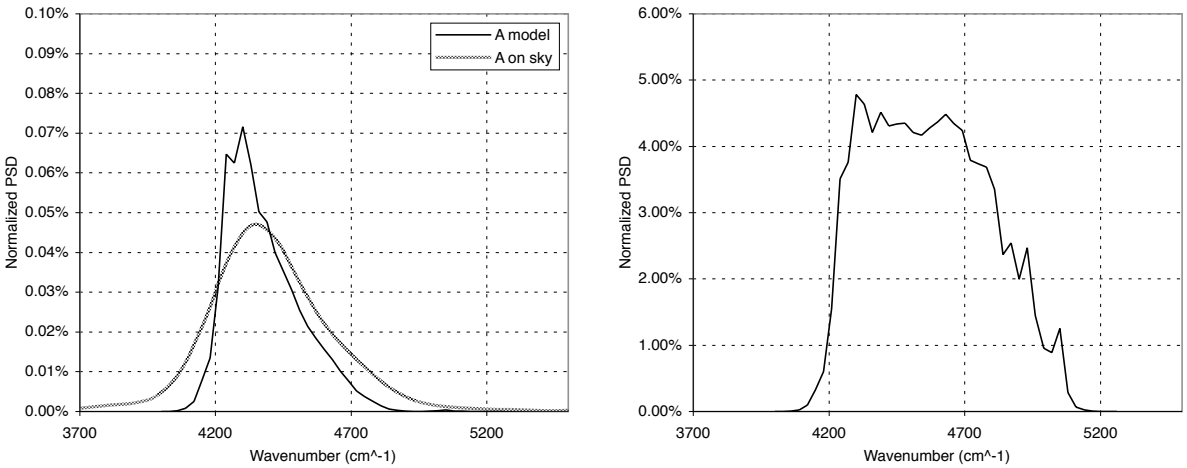

Figure 7. Left part: Model (black line) and observed (grey line) PSDs of α Cen A fringes on the 66m baseline (61m projected). The visibility loss for larger wave numbers is clearly visible compared to the right part of the figure, corresponding to the expected PSD shape for a zero baseline (equivalent to the filter transmission). The observed Fourier PSD, smoothed by the differential piston, shows the expected asymmetry. The models vertical scale is arbitrary.

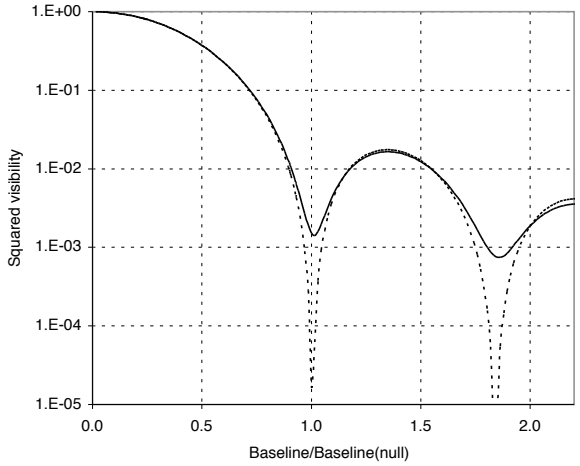

Figure 8. Comparison of a uniform disk visibility model in broadband regime including the bandwidth smearing effect (thick line) and the best matching monochromatic visibility model (dotted line). The horizontal axis values are expressed in units of the baseline resolving the source $B_{\rm null} = 1.22\,\lambda_0/\theta_{\rm UD}$ (first monochromatic null).

shape: the on-sky power spectrum is blurred by the differential piston and therefore appears "smoothed", but the characteristic asymmetry between lower and higher wave numbers is clearly visible. To account for the bandwidth smearing, the model visibility is computed for regularly spaced wave number spectral bins over the K band, and then integrated to obtain the model visibility.

The difference between the monochromatic and broadband visibility models is clearly visible on Fig. 8 (uniform disk case). This figure was computed using the transmission $T(\sigma)$ of the VINCI instrument and the effective temperature of the Sun. One remarkable property of the "smeared" V^2 curve is that it never goes down to zero for any baseline. Moreover, the position of the minima of the function are not strictly the same as the monochromatic model. Therefore, if the bandwidth smearing is not taken properly into account, this can lead to a wrong estimation of the expected visibility of the calibrator, in particular if it is resolved to a significant level. Consequently, this can create a systematic error on the estimation of the interferometric transfer function of the instrument that could be difficult to trace.

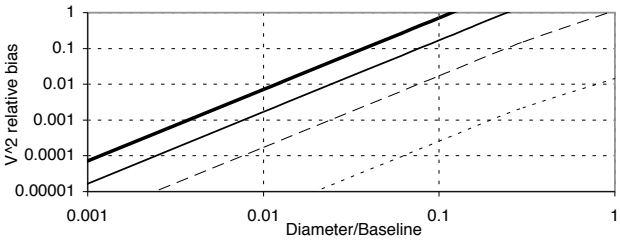

Figure 9. Relative bias introduced by the aperture smearing on the squared visibility. Three cases are plotted: the source is resolved at the first minimum of the visibility function (where we have $V^2 = 0.15\,\%$, thick line), $1\,\%$ (thin line), $10\,\%$ (dashed line) and $50\,\%$ (dotted line). These approximate values should not be used for calibration, but rather to decide if the aperture smearing effect can be considered negligible or not.

6.5. Aperture smearing

When the aperture of the light collectors is a significant fraction of the baseline, an effect similar to the bandwidth smearing appears on the visibility measurements. It comes from the fact that the baselines defined between different parts of the two primary mirrors cover a non-zero range of lengths and orientations. Without spatial filtering, the pupils of the two apertures can be matched in size and orientation at the recombination point. The interferences are created pairwise between each point of the pupils, with identical baseline and orientation for each pair of points. In VINCI, the principle is different as the spatial filtering is done *before* the recombination, and this results in an averaging of the electric fields over each pupil. The interferences being produced between these two averaged electric fields, this creates a smearing effect. This effect is not present if the spatial filtering happens *after* the beam combination.

As the angular resolution B/λ is actually a combination of the wavelength and the baseline length, several spatial frequencies are measured simultaneously by the beam combiner. In the case of observations conducted with the 8m Unit Telescopes and short baselines, this effect will have a significant impact on the visibility modeling. For observations on the 46 m UT1-UT2 baseline (ground length), we have a ratio $D/B \geq 17\,\%$. During observations, the projected baseline will always be shorter than the ground length, resulting in an increased and changing smearing effect. The visibility curve will thus be affected roughly by the same ammount by the bandwidth smearing ($\Delta\lambda/\lambda \approx 20\,\%$) and the aperture smearing. The integration of the aperture smearing effect when using single-mode fibers is relatively complex, as the apertures have to be weighted by the acceptance lobe of the fibers. Fig. 9 gives the relative bias on the squared visibility of the source due to the aperture smearing effect. The compared models (with and without aperture smearing) take both into account the bandwidth smearing effect, assuming the VINCI transmission and a blackbody source with $T_{\rm eff} = 5750\,\mathrm{K}$. The bias is always positive for the first lobe of the visibility function, but can be negative for higher order lobes. For the aperture to baseline ratio of the VLTI UT1-UT2 baseline ($17\,\%$), one can expect a relative bias of $+1.6\,\%$ for a V^2 value of $10\,\%$. Though relatively small, this bias is significantly larger than the statistical dispersion of the VINCI measurements on bright objects. An important aspect of the aperture smearing is that it is not attenuated using narrow spectral channels to make the observations, and should be considered for all high precision measurements.

7. CONCLUSION

The best results obtained with VINCI on bright stars are encouraging and show that an intrinsic precision of $\pm 0.1\%$ on the instrumental coherence factor μ is already feasible from the ground without external fringe tracking. But the intrinsic dispersion of this value is only half of the problem. The absolute calibration to recover the true visibility of the observed object can easily be the dominant source of uncertainty. Among the contributors to these systematic uncertainties, the fluctuations of the instrumental transfer function are likely to dominate the statistical dispersion in the final error bars of the visibility, especially if it is not sampled at a sufficienttly fast rate. Other effects, such as the bandwidth and aperture smearing, can also create biases on T^2, or on the modeling of the measured visibilities of the scientific targets. These factors combine to limit the

absolute precision of the visibility measurements achieved from the ground but part of them could also play a role for space based observations.

ACKNOWLEDGMENTS

P.K. acknowledges the partial support of the European Southern Observatory through a postdoctoral fellowship. D.S. acknowledges the support of the Swiss FNRS.

REFERENCES

1. Allison, F. 1924, *Astrophysical Journal*, **59**, 210
2. Arsenault, R., Alonso, J., Bonnet, H., et al. 2003, *Proc. SPIE*, **4839**, 174
3. Berger, J.-P., Haguenauer, P., Kern, P., et al. 2001, *Astronomy & Astrophysics*, **376**, 31
4. Coudé du Foresto, V., Ridgway, S., Mariotti, J.-M. 1997, *Astronomy & Astrophysics Suppl. Series*, **121**, 379
5. Claret, A. 2000, *Astronomy & Astrophysics*, **363**, 1081
6. Colavita, M. M. 1999, *Publications of the Astronomical Society of the Pacific*, **111**, 111
7. Coudé du Foresto, V., Perrin, G., Ruilier, C., et al. 1998, *Proc. SPIE*, **3350**, 856
8. Davis, J., Tango, W. J. & Booth, A. J. 2000, *Monthly Notices of the Royal Astronomical Society*, **318**, 387
9. Di Folco, E., Koehler, B., Kervella, P. et al. 2002, *Proc. SPIE*, **4838**, 1115
10. Gai, M., Bonino, D., Corcione, L., Delage, L., et al. 2003, *MmSAI*, **74**, 130
11. Hauschildt, P. H. & Baron, E. 1999, *J. Comp. Appl. Math*, **109**, 41
12. Kern, P., Malbet, F., Berger, J.-P., et al. 2003, *Proc SPIE*, **4838**, 312
13. Kervella, P., Coudé du Foresto, V., Glindemann, A., Hofmann, R. 2000,*Proc. SPIE*, **4006**, 31
14. Kervella, P., Gitton, Ph., Ségransan, D., et al. 2003, *Proc. SPIE*, **4838**, 858
15. Kervella, P., Thévenin, F., Morel, P., Bordé, P., & Di Folco, E. 2003, *Astronomy & Astrophysics*, **408**, 681
16. Kurucz, R. L. 1992, *IAU Symp. 149*: The Stellar Populations of Galaxies, **149**, 225
17. Linfield, R. P., Colavita, M. M. & Lane, B. F. 2001, *Astrophysical Journal*, **554**, 505
18. Perrin G. 2003, *Astronomy & Astrophysics*, **398**, 385
19. Tatulli, E., Mège, P., & Chelli, A. 2002, *Astronomy & Astrophysics*, **418**, 1179
20. Tango, W. J. & Davis, J. 2002, *Monthly Notices of the Royal Astronomical Society*, **333**, 642